Network desynchronization by non-Gaussian fluctuations

Jason Hindes[1], Philippe Jacquod[2,3], and Ira B. Schwartz[1]

[1] *U.S. Naval Research Laboratory, Code 6792, Plasma Physics Division, Washington, DC 20375, USA*
[2] *School of Engineering, University of Applied Sciences of Western Switzerland HES-SO, CH-1951 Sion, Switzerland and*
[3] *Department of Quantum Matter Physics, University of Geneva, CH-1211 Geneva, Switzerland*

Many networks must maintain synchrony despite the fact that they operate in noisy environments. Important examples are electric-power networks, where a rapidly increasing amount of power is supplied by renewable sources, which are known to exhibit fluctuations with broad tails. Such non-Gaussian fluctuations can result in rare network desynchronization. Here we build a general theory for inertial oscillator network desynchronization by non-Gaussian noise, which can be parameterized, for example, by input-power data. We compute the rate of desynchronization and show that higher-moments of noise enter at specific powers of coupling: either speeding up or slowing down the rate exponentially depending on how noise statistics match the statistics of a network's weakest stable mode. Finally, we introduce a technique that can be used to drastically reduce the number of equations needed to predict desynchronization in oscillator networks. For instance, when instability is associated with a single overloaded edge, the reduction is to one effective, noisy oscillator.

Networks of coupled oscillators form the foundation of complex physical, biological and technological systems[1], such as smart grids[2], Josephson junction arrays[3, 4], optical networks[5], biological networks[6–10], and coupled mechanical devices[11, 12]. From a deterministic viewpoint, most networks operate in stable attractor regimes, such as synchronized oscillations. However, in reality uncertainties and noise produce fluctuation patterns around an attractor, and may result in a loss of stability on long time scales observed as large fluctuations. As a consequence, much recent attention has been given to the effects of noise on networked oscillators, e.g., stochastic escape[14–18], noise cancellation[13], noise propagation[19–21], and synchronization[22, 23].

A motivating application for stochastic networked oscillators is that of fluctuating power grids driven by renewable energy sources, such as wind and solar. Such fluctuations are highly non-Gaussian[24–26], and may significantly impact power-grid stability[33–36]. Non-Gaussian noise is understood to exponentially alter switching rates for simple oscillator systems, including Josephson junctions and micro-mechanical oscillators[27–32]. Yet, predicting escape from synchrony in complex oscillator networks subjected to general noise patterns remains an outstanding problem.

The present letter takes a first step in this direction by analyzing desynchronization in networks of inertial oscillators driven by broadly distributed Poisson noise. Our approach is the first to connect desynchronization events to general noise statistics and network modes and subgraphs. We explicitly show how higher fluctuation moments control desynchronization rates near bifurcation points, both speeding up and slowing down rates depending on whether noise and network statistics have the same symmetry. Our analytical methods allow us to translate data into desynchronization rates, and explain how general noise tends to desynchronize particular network subgraphs.

Consider a model for N coupled phase oscillators with inertia. We assume that the acceleration of the ith oscillator's phase, ϕ_i, is determined by the velocity $v_i \equiv \dot{\phi}_i$, natural frequencies (input-power) P_i, and coupling between oscillators $\sum_j K_{ij}\sin(\phi_j - \phi_i)$, such that it satisfies the swing equation for synchronous machines:

$$M\dot{v}_i + \gamma v_i = P_i + \sum_j K_{ij}\sin(\phi_j - \phi_i), \qquad (1)$$

where M and γ are inertial and damping constants[37]. Equation (1) is an idealized model for electric power networks[38, 39], which we discuss as an illustration. In what follows, we take $K_{ij} = KA_{ij}$, where A_{ij} is a symmetric adjacency matrix[14].

In order to study the effects of non-Gaussian power fluctuations on Eq.(1), we take the input power to be[37]

$$P_i(t) = \bar{P}_i + p_i(t), \qquad (2)$$

where the fluctuation $p_i(t)$ has over-damped dynamics

$$\dot{p}_i = -\alpha p_i + \xi_i(t), \qquad (3)$$

with a damping rate α and stochastic drive $\xi_i(t)$[13, 14, 16, 18, 40]. We are particularly interested in cases where $p_i(t)$ exhibits large, intermittent spikes[35] at measurable rates and amplitudes. Such patterns are seen in the output power from wind and solar sources[24–26]. The non-Gaussian features can be captured by tracking the change in power over fixed time-intervals[25]. For example, similar to [21], we consider the average output power from 12 wind turbines in northern Germany at one second resolution, and plot the distribution of power increments, $g = p_i(t + 1) - p_i(t)$, or pr(g). The resulting histogram is shown in Fig.1(a), which is highly non-Gaussian – e.g., the distribution's fourth moment is much larger than a Gaussian with the same variance.

Building a noise model with the measured increment distribution, we assign an independent Poisson pulse[41] to every bin, b, in the histogram. The pulse amplitude, g_b, is equal to the bin average, and the rate is $\nu_b = \text{pr}(g_b)/\tau$, where τ is the time resolution of the data.
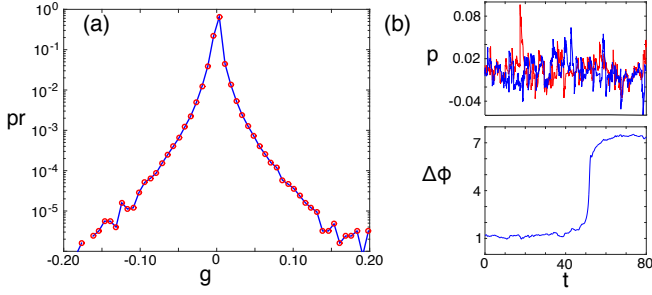
FIG. 1. Non-Gaussian power fluctuations. (a) Wind turbine power-increment distribution[21]. (b) Fluctuation time series (seconds) given independent and identically distributed Poisson fluctuations for a 30-node network. Amplitudes and rates are taken from (a). Power fluctuations for two oscillators are shown in blue and red (top). Phase-difference, $\Delta\phi$, between the oscillators (lower). $\alpha = 1.0$ and $\tau = 0.1$[42].

Given this choice, a pulse occurs on average every τ units of time. More generally, let there be $\mathcal{M}$ arbitrary power increments, such that the amplitude for the bth increment on the ith oscillator is g_{ib}, where $b \in \{1, 2, ..., \mathcal{M}\}$. By denoting the time at which the nth such increment occurs as $t_{ib}[n]$, the stochastic drive $\xi_i(t)$ can be represented by Dirac delta functions, $\xi_i(t) = \sum_{bn} g_{ib}\delta(t - t_{ib}[n])$ [41]. Because the noise is Poisson, the difference between $t_{ib}[n]$ and the next increment time, $t_{ib}[n + 1]$, is exponentially distributed with a rate ν_{ib}. As is customary, we assume that the time average of the power fluctuations is zero for each oscillator, $\sum_b g_{ib}\nu_{ib} = 0$, and the network's average input power is zero $\sum_i \bar{P}_i = 0$. An example time series given our model is shown in Fig.1(b).

Large fluctuation picture of desynchronization. When the coupling constant K is sufficiently large, a synchronized state is stable, which is a fixed point of Eq.(1) – depending on network topology and the distribution of $\bar{P}_i$ [37]. In general, this stable phase-locked state (PLS) emerges through an inverse saddle-node bifurcation[43] as K is increased, implying the existence of unstable, saddle phase-locked states. As has been shown recently, Gaussian noise on Eq.(1) causes networks to fluctuate to these saddles [14, 16, 18], at which time they can desynchronize: either by undergoing a large phase slip upon returning to the PLS modulo 2π, as shown in Fig.1(b)(lower), or exiting its basin of attraction altogether. Such noise-induced desynchronization, whereby fluctuations drive oscillator networks to saddle points, are examples of the general phenomenon of basin-escape (switching) [44, 45].

Given the non-Gaussian noise discussed above, our strategy is to construct the most-likely (optimal) path from PLS to saddles, whereby fluctuations and the network dynamics couple together in such a way as to maximize the probability of desynchronization. When desynchronization is rare, the optimal path is describable in terms of analytical mechanics. This approach is valid as long as typical fluctuations are small compared to the distances to saddles.

The Fokker-Planck equation[46] for the network probability distribution, $\rho(\boldsymbol{\phi}, \mathbf{v}, \mathbf{p}, t)$, is

$$\frac{\partial \rho}{\partial t} = \sum_i \Bigg[-\frac{\partial}{\partial \phi_i}\big[v_i\rho\big] + \frac{\partial}{\partial p_i}\big[\alpha p_i \rho\big] \tag{4}$$

$$-\frac{\partial}{\partial v_i}\Big[\Big(-\frac{\gamma v_i}{M} + \frac{1}{M}\big(P_i + \sum_j K_{ij}\sin(\phi_j - \phi_i)\big)\Big)\rho\Big]$$

$$+ \sum_b \nu_{ib}\Big[\rho(\boldsymbol{\phi}, \mathbf{v}, \mathbf{p} - g_{ib}\mathbf{1}_i) - \rho(\boldsymbol{\phi}, \mathbf{v}, \mathbf{p})\Big]\Bigg],$$

where the vector $\mathbf{1}_i = \langle 0_1, 0_2, .., 1_i, .., 0_N\rangle$. We can isolate the exponential tails of the distribution associated with rare events by substituting a WKB ansatz, $\rho(\boldsymbol{\phi}, \mathbf{v}, \mathbf{p}, t) = B\exp\{-S(\boldsymbol{\phi}, \mathbf{v}, \mathbf{p}, t)\}$, into Eq.(4), assuming $S(\boldsymbol{\phi}, \mathbf{v}, \mathbf{p}, t) \gg 1$, and keep the leading order terms in $\partial_{\boldsymbol{\phi}}S$, $\partial_{\boldsymbol{v}}S$, and $\partial_{\boldsymbol{p}}S$ [46, 47]. This approximation converts Eq.(4) to a Hamilton-Jacobi equation (HJE) for the probability exponent, $S(\boldsymbol{\phi}, \mathbf{v}, \mathbf{p}, t)$, called the *action*, in terms of $\boldsymbol{\phi}$, $\mathbf{v}$, $\mathbf{p}$, and their conjugate momenta, $\boldsymbol{\lambda}^\phi \equiv \partial_{\boldsymbol{\phi}}S$, $\boldsymbol{\lambda}^v \equiv \partial_{\boldsymbol{v}}S$, and $\boldsymbol{\lambda}^p \equiv \partial_{\boldsymbol{p}}S$. The network Hamiltonian is

$$H(\boldsymbol{\phi}, \mathbf{v}, \mathbf{p}, \boldsymbol{\lambda}^\phi, \boldsymbol{\lambda}^v, \boldsymbol{\lambda}^p) = \sum_i \Bigg[\lambda_i^\phi v_i - \alpha p_i \lambda_i^p$$

$$+ \sum_b \nu_{ib}\Big(\exp\{g_{ib}\lambda_i^p\} - 1\Big) +$$

$$\frac{\lambda_i^v}{M}\Big(-\gamma v_i + \bar{P}_i + p_i + \sum_j K_{ij}\sin(\phi_j - \phi_i)\Big)\Bigg]. \tag{5}$$

As in mechanics, the phase-space dynamics satisfy Hamilton's equations [48, 49], with a stationary action

$$S(\boldsymbol{\phi}, \mathbf{v}, \mathbf{p}) = \sum_i \Bigg[\int \lambda_i^\phi d\phi_i + \int \lambda_i^v dv_i + \int \lambda_i^p dp_i \Bigg]. \tag{6}$$

Solutions are computable numerically, subject to boundary conditions[50]. From the action, the expected waiting time (or inverse rate) for desynchronization is $\ln\langle T\rangle \cong S(\boldsymbol{\phi}^s, \mathbf{0}, \mathbf{0}) + $constant [44, 45, 51].

Using our desynchronization mechanics, let us first consider the optimal path (OP) from PLS, $\boldsymbol{\phi}^*$, to saddles, $\boldsymbol{\phi}^s$, near the saddle-node bifurcation (SN). We denote the critical coupling K_{SN}, where $K = K_{\text{SN}}[1 + \kappa]$. When $\kappa \ll 1$, the dynamics slows onto a one-dimensional manifold with universal properties. As we will show, statistical moments of the power fluctuations first contribute to the action at specific powers of κ, from which we can calculate their effects on desynchronization rates. In the following, we assume that noise for all nodes is independent and identically distributed, for illustration purposes, and we drop the subscript i in ν, g and μ.

First, we construct the lowest-order solution, and thereby demonstrate our natural expansion in $\kappa^{1/2}$. Higher order terms are constructed in the SM[48]. From the fixed-point boundary conditions we expand

ϕ^* and ϕ^s around the SN value, ϕ^{SN}, in powers of κ. At the saddle-node bifurcation, the Fiedler mode[52] of the Laplacian $L_{ij}(\phi^*) = A_{ij}\cos(\phi_j^* - \phi_i^*) - \delta_{ij}\sum_k A_{ik}\cos(\phi_j^* - \phi_i^*)$, has zero eigenvalue. In general, the Fiedler mode is the slowest mode of the Laplacian, $L_{ij}(\phi^*)$, and we denote it r_i. In terms of r_i, $\phi_i^* = \phi_i^{SN} - C\kappa^{1/2}r_i$ and $\phi_i^s = \phi_i^{SN} + C\kappa^{1/2}r_i$, where[48]:

$$C = \sqrt{\frac{2|\sum_{ij}A_{ij}\sin(\phi_j^{SN}-\phi_i^{SN})r_i|}{|\sum_{ij}A_{ij}\sin(\phi_j^{SN}-\phi_i^{SN})[r_j-r_i]^2r_i|}}. \quad (7)$$

Since the sums in Eq.(7) appear when considering the noise moments, we write $C \equiv \sqrt{2R_0/R_2}$. Next, we notice that the phases emerging from the SN can be written in terms of a coordinate $x(t)$, $\phi_i(t) = \phi_i^{SN} + C\kappa^{1/2}r_ix(t)$, where $x \in [-1,1]$. Substituting this form into Hamilton's equations, and collecting terms at order κ, we find[48]:

$$\frac{v_i}{r_i} = \frac{K_{SN}\kappa R_0[1-x^2]}{\gamma}, \qquad \frac{p_i}{r_i} = 2K_{SN}\kappa R_0[1-x^2],$$

$$\frac{\lambda_i^\phi}{r_i} = \frac{2K_{SN}\kappa R_0\gamma\alpha^2[1-x^2]}{\mu_2}, \quad \frac{\lambda_i^v}{r_i} = \frac{2K_{SN}\kappa R_0M\alpha^2[1-x^2]}{\mu_2},$$

$$\frac{\lambda_i^p}{r_i} = \frac{2K_{SN}\kappa R_0\alpha[1-x^2]}{\mu_2}, \quad \dot{x} = \frac{K_{SN}\kappa^{1/2}\sqrt{2R_0R_2}[1-x^2]}{2\gamma},$$

$$(8)$$

where $\mu_2 = \sum_b \nu_b g_b^2$ is the fluctuation variance. From Eqs.(6) and (8), we get

$$S(\phi^s, \mathbf{0}, \mathbf{0}) = \frac{8\sqrt{2}K_{SN}\kappa^{3/2}\gamma\alpha^2R_0^{3/2}}{3R_2^{1/2}\mu_2}. \quad (9)$$

The structure of Eq.(9) is interesting. The action is proportional to the damping rate for power-fluctuations squared, implying that doubling the rate, increases the time-scale for desynchronization as $\langle T \rangle \to \langle T \rangle^4$. What's more, each node's contribution is proportional to μ_2^{-1}, and hence power-increment distributions with the same variance produce the same rate of desynchronization at lowest order in κ. The effects of higher fluctuation moments must, therefore, appear at higher powers of κ.

Continuing our construction at higher-powers in κ, we notice that the lowest-order contribution to the action from the nth moment of the fluctuations, $\mu_n = \sum_b \nu_b g_b^n$, is determined by the zero-energy condition, $H(\phi, \mathbf{v}, \mathbf{p}, \lambda^\phi, \lambda^v, \lambda^p) = 0$, at $\mathcal{O}(\kappa^n)$ [49]. Surprisingly, such contributions, $\Delta^{(n)}S$, only depend on Eq.(8) and can be calculated[48]:

$$\Delta^{(n)}S = -\frac{\mu_n[\sum_i r_i^n]}{\mu_2^n} \cdot \kappa^{n-\frac{1}{2}}K_{SN}^{n-1} \cdot \quad (10)$$

$$\frac{2^{n+\frac{1}{2}}\gamma\alpha^nR_0^{n-\frac{1}{2}}\int_{-1}^1(1-x^2)^{n-1}dx}{R_2^{1/2}n!}.$$

Equation (10) is particularly useful for comparing non-Gaussian and Gaussian white noise (GWN) effects; in
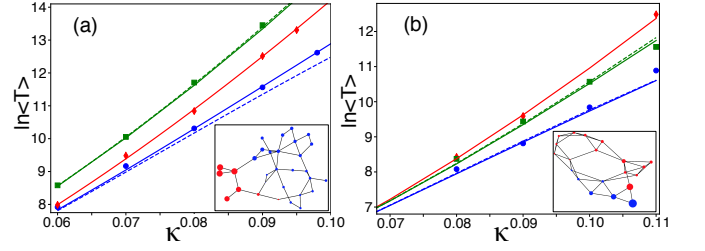

FIG. 2. Effect of non-Gaussian noise on desynchronization times. Points denote Monte-Carlo simulations and solid lines denote least-action computations, Eq.(6). Fluctuations follow the color scheme: Gaussian (red), positively skewed (green), and symmetric wind turbine (blue)– all with the same variance. Dashed lines are predictions from Eq.(10). (a) Negatively skewed network. (b) Positively skewed network.

the latter, the stochastic drive in Eq.(3), is replaced by a Gaussian process with time-correlation $\langle \xi_i(t)\xi_j(t') \rangle = \mu_2\delta_{ij}\delta(t - t') \forall\{i, j\}$. Because the action for GWN is equivalent to keeping only the variance in the Hamiltonian [46, 49], Eq.(10) represents the correction to the GWN action from fluctuations with a first non-zero moment μ_n ($n > 2$). Since the Fiedler mode has a zero component sum, the balance between its positive and negative components clearly affects Eq.(10) when the first non-Gaussian moment is odd. Quite surprisingly, for $n = 3$, it is the product of the skewness of the noise distribution with the skewness of the Fiedler mode that determines if the non-Gaussianity increases or decreases desynchronization rates. Additionally, the desynchronization rate exhibits a critical behavior characterized by a spectrum of critical exponents $n - \frac{1}{2}$ depending on the nth moment of the noise distribution.

Two examples are shown in Fig.2, where we compare desynchronization times for GWN (red), positively skewed $\mu_3 > 0$ (green)[48], and wind turbine (blue) fluctuations– all with the same variance. Solid lines denote Eq.(6) computations, while points indicate Monte-Carlo simulations[48]. The dashed lines in green and blue denote the Gaussian-action[48] plus Eq.(10), which is in good agreement (in most cases hard to distinguish). The networks are drawn in each subpanel, where nodes are blue if $r_i > 0$ and red if $r_i < 0$; sizes are proportional to $|r_i|$. In Fig.2(a), the network is negatively skewed, $\sum_i r_i^3 < 0$, and hence desynchronization occurs at an exponentially slower rate. In contrast in Fig.2(b) the network is positively skewed, and shows the opposite effect. For both networks, symmetric power fluctuations ($\mu_3 \approx 0$) produce an increase in the rate (blue is always under the red).

Synchronized subgraph approximation. Since the Fiedler mode is the weakest stable mode of a network, and we have shown that rare desynchronization occurs along it[48], nodes that are topologically nearby and have similar Fiedler-mode values, do not tend to separate during desynchronization. What's more, we notice that the SN bifurcation occurs with very nearly (and often exact) symmetry in the Fiedler mode, where $r_i \cong r_j$ for
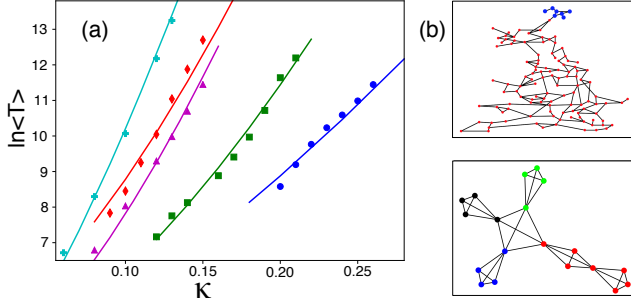
FIG. 3. Desynchronization times predicted assuming synchronized subgraphs (Eq.(12) and its generalization[48]); (a) UK grid with one overloaded edge (green), a 50-node tree (red), a 100-node tree (blue), a block network (cyan), and the UK grid without symmetry (magenta). Solid lines denote computations, while points correspond to Monte-Carlo. (b) Synchronized subgraphs for the UK grid (top), and the block network (bottom). Subgraphs are drawn with different colors.

some (i, j) [52]. These observations can be used as a basis for finding much lower-dimensional desynchronization pathways, which we call the synchronized subgraph approximation (SSA).

First, our intuition can be made exact for networks where the SN corresponds to a single (overloaded) edge with a phase-difference $\pi/2$; such is always the case for trees and frequently the case for sparse networks[43]. For these *single-cut saddle-nodes* (SCSN), we can always construct a SSA: where the network splits into exactly *two subgraphs*, and the nodes within each remain synchronized on average. If we denote the two subgraphs divided by the overloaded edge $\mathcal{S}_1$ and $\mathcal{S}_2$, then we can reduce Hamilton's equations to a single noisy oscillator system in relative phase-space coordinates [48]:

$$\dot{V} = \frac{1}{M}\left[-\gamma V + P + \frac{K_{\mathrm{SN}}N}{|\mathcal{S}_1||\mathcal{S}_2|}\big(1 - (1+\kappa)\cos\{\Psi\}\big)\right]$$

$$\dot{P} = -\alpha P + \sum_m \nu_m g_m\Big[e^{g_m\Lambda_P/|\mathcal{S}_1|} - e^{-g_m\Lambda_P/|\mathcal{S}_2|}\Big]$$

$$\dot{\Lambda}_\Psi = -\frac{K_{\mathrm{SN}}(1+\kappa)}{M}\frac{N}{|\mathcal{S}_1||\mathcal{S}_2|}\Lambda_V \sin\{\Psi\}, \quad V = \dot{\Psi}$$

$$\dot{\Lambda}_V = -\Lambda_\Psi + \frac{\gamma}{M}\Lambda_V, \qquad \dot{\Lambda}_P = \alpha\Lambda_P - \frac{1}{M}\Lambda_V \quad (11)$$

The system Eqs.(11) is closed, since $K_{\mathrm{SN}} = |\sum_{i\in\mathcal{S}_1}\bar{P}_i|$ for SCSN [48, 53]. Also, it is parameterized by κ, N, and the sizes of the two subgraphs, $|\mathcal{S}_1|$ and $|\mathcal{S}_2|$, but is otherwise *independent of topology*. The action corresponds to a single oscillator:

$$S(\Psi, V, P) = \int \Lambda_\Psi d\Psi + \int \Lambda_V dV + \int \Lambda_P dP. \quad (12)$$

A comparison of desynchronization times with the SSA for three different networks with a SCSN are shown in Fig.3(a) (red, blue, and green) where $N \sim \mathcal{O}(100)$. In particular, the UK power grid is shown in green, and its two

subgraphs are drawn in the top of Fig.3(b). Computations are shown with sold lines (Eq.12) and Monte-Carlo with points[48]. Examples show quantitative agreement, despite two-orders of magnitude reduction in the desynchronization dynamics.

Similarly, the SSA can be easily applied to networks without a SCSN, but where there is an exact symmetry in the Fiedler mode. The algorithm for constructing reduced Hamilton's equations for general cases is given in the SM[48]. An example is shown in Fig.3(a) in cyan for a block network, and its subgraphs drawn in Fig.3(b)– the lower panel. In this case, the network splits into four subgraphs at bifurcation, and therefore the SSA consists of four effectively coupled oscillators. Lastly, the SSA can be applied to networks whose Fiedler modes do not have exact symmetry, by partitioning the network into subgraphs with approximately uniform Fiedler-mode values (within some tolerance). An example is shown in Fig.3(a) (magenta), again for the UK power grid, but in this case, with a different distribution of $\bar{P}_i$ and without exact symmetry at bifurcation. The solid line represents a SSA assuming 20 subgraphs[48].

In this letter, we analyzed desynchronization in complex oscillator networks by non-Gaussian noise. It is often thought that broad-tailed fluctuations perturb dynamical systems more strongly. However, we found that such noise does not always increase the rate of network desynchronization; the latter depends on whether higher-moments of fluctuations and a network's weakest stable mode have the same sign, and therefore represents a topological effect as well as a noise effect. Our approach was based on arbitrarily distributed Poisson noise, which can be easily fit to power-increment data from renewable energy sources, as we demonstrated. Lastly, we developed a reduction technique based on the observation that noise tends to effectively desynchronize only certain network subgraphs specified by a network's weakest stable mode. Such a reduction should be valuable for studying rare processes in high-dimensional oscillator networks more broadly, where predicting rare events is notoriously difficult.

In addition, our approach revealed a spectrum of scaling exponents that determine at what powers in the coupling the nth moment of noise contributes to desynchronization rates. Our results are general for escape through a saddle. However, our method can be generalized to rare events induced by non-Gaussian noise in other dynamical processes in networks including: extinction[54, 55], switching[56], and more general oscillator transitions[57].

Supplementary material

I.   Simulations

Monte-Carlo simulations were performed using a combination of Gillespie's algorithm for power fluctuations, p_i, and Euler's method for integrating the differential equations between reaction times. C++ code is available upon request. For illustration, we assume that the noise is independent and identically distributed (iid) for each node. The stochastic rate for the *next reaction* is $\mathcal{R} = \sum_{i,m} \nu_{im} = N \sum_m \nu_m$. The next reaction time is stochastically selected $\Delta T = -\ln(r_1)/\mathcal{R}$, where r_1 is a uniformly distributed random number over the unit interval. Since the noise is *iid*, the node which receives the increment is selected uniformly at random from the N nodes. Another random number is generated, $\mathcal{P} = r_2 \sum_m \nu_m$, where r_2 is a uniformly distributed random number over the unit interval. The nth increment is chosen if $\sum_{m=1}^{n-1} \nu_m < \mathcal{P} < \sum_{m=1}^{n} \nu_m$. Equations (1-3) are integrated with Euler's method from t to $t+\Delta T$ with time steps $dt = 4*10^{-5}$, at which time the selected node, e.g,. i, has its power incremented: $p_i \to p_i + g_n$. On the other hand, for Gaussian noise the Euler-Milstein method was used with $dt = 4*10^{-5}$.

The wind-turbine data was taken from [21]. The data consists of power measurements at 1-second resolution for 12 turbines, each rated at 2MW. We averaged over the available data at each time step and histogrammed the power increments $p(t+1) - p(t)$ using 60 uniformly spaced bins ($\mathcal{M} = 60$). The result is Fig.1(a). In order to make desynchronization less rare, we artificially increased the rate, such that $\sum_m \nu_m = 10s^{-1}$, not $1s^{-1}$. For reference, the noise variance for *iid* is $\mu_2 = 5.8317*10^{-4}s^{-1}$. For skewed noise comparisons, we chose a simple two-pulse model: $\nu_m \in \{10, 3.33333\}$ and $g_m \in \{-0.0038183, 0.0114549\}$, which has the same variance.

Each Monte-Carlo point in Figs.2-3 represent the log of the average of 200 slip times – defined as the time it takes to see a phase difference greater than 2π develop between any connected oscillators. Each of the slips were generated from the phase-locked state initial conditions and with different random number seeds. All simulations in Fig.3 were done with skewed noise except for the block network (cyan), for which we used the wind-turbine noise.

All networks are drawn in the text, except for the two random trees in Fig.3. Topologies, $\bar{P}_i$, and α are available upon request for all examples. In Fig.2(a), we note that the network considered is a 30-node IEEE-test-bus network (not mentioned in the main text).

II.   Finding the saddle-node bifurcation

The coupling at which the saddle-node occurs, K_{SN}, can be computed numerically by solving the following $N+1$ equations with a quasi-Newton method:

$$0 = \bar{P}_i + K_{\mathrm{SN}} \sum_j A_{ij} \sin(\phi_j^{SN} - \phi_i^{SN}) \ \ \forall i \qquad (13)$$

$$0 = z; \qquad (14)$$

where z is the second smallest (in magnitude) eigenvalue of the Laplacian matrix $L_{ij}(\boldsymbol{\phi}^{SN}) = A_{ij} \cos(\phi_j^{SN} - \phi_i^{SN}) - \delta_{ij} \sum_k A_{ik} \cos(\phi_j^{SN} - \phi_i^{SN})$.

III.   Computing optimal paths

Optimal paths for rare desynchronization satisfy Hamilton's equations:

$$\dot{\phi}_i = v_i, \qquad (15)$$

$$M\dot{v}_i = -\gamma v_i + p_i + \bar{P}_i + K \sum_j A_{ij} \sin(\phi_j - \phi_i), \quad (16)$$

$$\dot{p}_i = -\alpha p_i + \sum_b \nu_{ib} g_{ib} \exp\{g_{ib}\lambda_i^p\}, \qquad (17)$$

$$\dot{\lambda}_i^\phi = -\frac{K}{M} \sum_j A_{ij} \cos(\phi_j - \phi_i)[\lambda_j^v - \lambda_i^v], \qquad (18)$$

$$\dot{\lambda}_i^v = -\lambda_i^\phi + \frac{\gamma}{M}\lambda_i^v, \qquad (19)$$

$$\dot{\lambda}_i^p = \alpha\lambda_i^p - \lambda_i^v/M. \qquad (20)$$

Numerical solutions of Eqs.(15-20) were found using the Iterative-Action-Minimization-Method (B. S. Lindley and I. B. Schwartz, Physica D **255**, 22 (2013)) with fixed-point boundary conditions. Example Matlab code can be found in the supplementary material of (J. Hindes and I. B. Schwartz, EPL **120**, 56004 (2017)), for example, and is available upon request. The method requires a trial solution. For small κ we used Eqs.(8) from the main text, and then bootstrapped to other regions of parameter space.

IV.   Fixed points

In order to calculate optimal paths as a function of the distance to bifurcation κ, where $K = K_{\mathrm{SN}}[1 + \kappa]$, we first calculate the fixed points of Eq.(1) in powers of κ. Let us substitute $\phi_i^* = \phi_i^{SN} + \kappa^{1/2}q_i + \kappa w_i + ...$ into Eq.(1), given $\dot{v}_i = 0$ and $v_i = 0 \ \forall i$. Note, the sub(super)-script SN implies evaluation at the saddle-node. Our goal is to find q_i. At $\mathcal{O}(\kappa^{1/2})$ we find the equation

$$0_i = \sum_j A_{ij} \cos(\phi_j^{SN} - \phi_i^{SN})[q_j - q_i], \qquad (21)$$

which expresses the saddle-node condition that the network Laplacian has a Fiedler mode with eigenvalue zero. Hence, we may write $q_i = -Cr_i$, where r_i is the Fiedler

mode at bifurcation and C is a constant that we wish to determine. Continuing to $\mathcal{O}(\kappa)$, gives

$$0_i = \sum_j A_{ij} \cos(\phi_j^{SN} - \phi_i^{SN})[w_j - w_i]$$
$$+ \sum_j A_{ij} \sin(\phi_j^{SN} - \phi_i^{SN})$$
$$- \frac{C^2}{2} \sum_j A_{ij} \sin(\phi_j^{SN} - \phi_i^{SN})[r_j - r_i]^2. \quad (22)$$

If we take the product of Eq.(22) with r_i, sum over i, and solve for C, we get Eq.(7) from the main text. This is easy to see by expanding w_i in the eigenmodes of the Laplacian. In Eq.(22), the component parallel to r_i vanishes from the saddle-node condition, while all other components vanish due to orthonormality. Note: there are two possible solutions for C: a stable phase-locked state (positive), and a saddle (negative). Given the definitions in the main text, the Fiedler value can be shown to be

$$z = -\sqrt{2R_0 R_2}\kappa^{1/2}, \quad (23)$$

by an analogous expansion.

1. Single-cut saddle node

The procedure outlined above can be carried out indefinitely. Here, we restrict ourselves to a particular class of saddle-node bifurcations, which we call single-cut saddle-nodes (SCSN). In this special case, a single line becomes overloaded at bifurcation, and such a line is a cut edge of the network specified by the adjacency matrix. The edge partitions the network into exactly two subgraphs (denoted $\mathcal{S}_1$ and $\mathcal{S}_2$), whose nodes only share one edge (the cut edge) in common. For example, tree networks always have SCSN.

Networks with SCSN have useful properties. For instance, K_{SN} can be determined by summing Eq.(1) over all nodes in $\mathcal{S}_1$ (or $\mathcal{S}_2$), given $\dot{v}_i = 0$ and $v_i = 0 \; \forall i$:

$$0 = \sum_{i \in \mathcal{S}_1} P_i + K_{\mathrm{SN}} \sum_{i \in \mathcal{S}_1, j} \sin(\phi_j^{SN} - \phi_i^{SN}). \quad (24)$$

Only one term survives in the second sum in Eq.(24): corresponding to the cut edge connecting $\mathcal{S}_1$ and $\mathcal{S}_2$– because sine is an odd function. Moreover the phase difference for the cut edge is $\phi_j^{SN} - \phi_i^{SN} = -\pi/2$. This latter property can be shown from the saddle-node condition and the fact that for SCSN $r_i = \sqrt{|\mathcal{S}_2|/[N|\mathcal{S}_1|]}$ if $i \in \mathcal{S}_1$, and $r_i = -\sqrt{|\mathcal{S}_1|/[N|\mathcal{S}_2|]}$ if $i \in \mathcal{S}_2$. Note: the specifications for $\mathcal{S}_1$ and $\mathcal{S}_2$ are given by the convention that the node in $\mathcal{S}_1$ connected to $\mathcal{S}_2$ along the cut edge has a larger phase than its counterpart in $\mathcal{S}_2$. Therefore,

$$K_{\mathrm{SN}} \overset{\mathrm{SCSN}}{=} \sum_{i \in \mathcal{S}_1} \bar{P}_i, \quad (25)$$

as first noted for trees in [53].

Using the stated SCSN properties, it is straightforward to show that

$$\phi_i^s - \phi_i^* = 2Cr_i\kappa^{1/2}\left[1 - \frac{5}{12}\kappa + \frac{43}{160}\kappa^2 + ...\right], \quad (26)$$

by expanding the fixed-point conditions to higher orders in κ. In Fig.4(a) we plot the mean (blue) and standard deviation (red) of the error-vector, $\mathrm{Error}_i = [\phi_i^s - \phi_i^* - 2Cr_i\kappa^{1/2}(1 - \frac{5}{12}\kappa + \frac{43}{160}\kappa^2)]/r_i$ for an example SCSN shown in Fig.4(b). We can see that the fixed-point expression Eq.(26) is accurate to $\mathcal{O}(\kappa^{7/2})$ and is parallel to r_i. The fixed points were computed numerically with the choice of zero-average-phase $\langle\phi_i^s\rangle = \langle\phi_i^*\rangle = 0$.
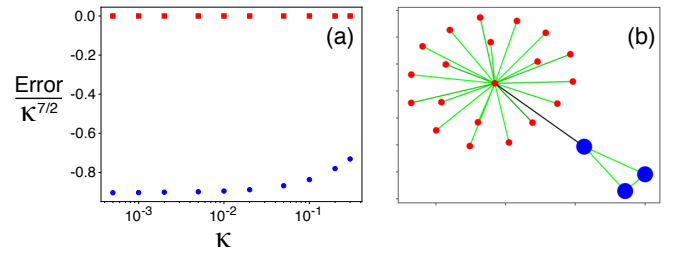

FIG. 4. Error scaling of Eq.(26) for a SCSN (a) mean (blue) and standard-deviation (red) of the error divided by $\kappa^{7/2}$. (b) example network.

V. Near bifurcation paths

Using the fixed-point boundaries expressed in powers of κ, we can construct the optimal paths for sufficiently small κ. To make the calculation simpler, at this point we restrict ourselves to *iid* power fluctuations, and drop the node-subscript i in the noise moments, μ. As mentioned in the main text, at lowest order in κ, we substitute the ansatz $\phi_i(t) = \phi_i^{SN} + C\kappa^{1/2}r_i x(t) + ...$ into Eqs.(15-20). For the other phase-space variables, we have the general expansions:

$$v_i = \sum_m v_{i,m}\kappa^{\frac{m}{2}}, \qquad p_i = \sum_m p_{i,m}\kappa^{\frac{m}{2}}$$
$$\lambda_i^\phi = \sum_m \lambda_{i,m}^\phi \kappa^{\frac{m}{2}}, \qquad \lambda_i^v = \sum_m \lambda_{i,m}^v \kappa^{\frac{m}{2}}$$
$$\lambda_i^p = \sum_m \lambda_{i,m}^p \kappa^{\frac{m}{2}}, \quad (27)$$

where $m = 2, 3, ...$ When $m = 2$, we assume that all variables are parallel to the Fiedler mode according to $v_{i,2} = a_v(x)r_i$, $p_{i,2} = a_p(x)r_i$, $\lambda_{i,2}^\phi = a_\lambda^\phi(x)r_i/\mu_2$, $\lambda_{i,2}^v = a_\lambda^v(x)r_i/\mu_2$, and $\lambda_{i,2}^p = a_\lambda^p(x)r_i/\mu_2$.

We note that since $\dot{x} = a_v(x)\kappa^{\frac{1}{2}}/C$, time-derivatives for phase-space variables other than ϕ are $\mathcal{O}(\kappa^{\frac{3}{2}})$, and

so the LHS of Eqs.(16-20) can be ignored at $\mathcal{O}(\kappa)$. By substituting the expansion into Eqs.(16-17) and Eqs.(19-20), we find the following relations for $\mathcal{O}(\kappa)$:

$$-\gamma a_v + a_p = -K_{\mathrm{SN}}(1-x^2)\sum_{ij}A_{ij}\sin(\phi_j^{SN}-\phi_i^{SN})r_i \tag{28}$$

$$\alpha a_p = a_\lambda^p \tag{29}$$

$$a_\lambda^\phi = \frac{\gamma}{M}a_\lambda^v \tag{30}$$

$$\alpha a_\lambda^p = \frac{1}{M}a_\lambda^v. \tag{31}$$

One more equation is needed to close the system. We use the zero-energy condition $H(\boldsymbol{\phi},\mathbf{v},\mathbf{p},\boldsymbol{\lambda}^\phi,\boldsymbol{\lambda}^v,\boldsymbol{\lambda}^p)=0$, at $\mathcal{O}(\kappa^2)$, which results in

$$0 = a_\lambda^\phi a_v - \alpha a_\lambda^p a_p + \frac{[a_\lambda^p]^2}{2}. \tag{32}$$

Solving for the non-zero solution gives Eqs.(8) from the main text. Note: we have assumed that the product, $\sum_{ij}A_{ij}\sin(\phi_j^{SN}-\phi_i^{SN})r_i$, is negative in writing Eqs.(8), given our sign convention. This property appears to be general for the SN. Hence, $R_0 = -\sum_{ij}A_{ij}\sin(\phi_j^{SN}-\phi_i^{SN})r_i = |\sum_{ij}A_{ij}\sin(\phi_j^{SN}-\phi_i^{SN})r_i|$.

1. Single-cut saddle node

As with the fixed-point boundaries in Sec.IV, we restrict ourselves to SCSN for higher-order OPs, since the results are comparatively simple. First, we start with the ansatz $\phi_i(x) = \phi_i^{SN} + Cx(t)r_i\kappa^{1/2}[1-\frac{5}{12}\kappa]$, from Eq.(26). The next order in κ requires substituting this ansatz, as well as the general expansion Eqs.(27) into Eqs.(16-17) and Eqs.(19-20) and collecting terms of $\mathcal{O}(\kappa^{3/2})$. As noted in the previous section, the relevant time derivatives are at lowest order $\mathcal{O}(\kappa^{3/2})$:

$$\frac{\dot{v}_i}{r_i} = \frac{\kappa^{\frac{3}{2}}}{C}\frac{da_v}{dx}a_v(x), \qquad \frac{\dot{p}_i}{r_i} = \frac{\kappa^{\frac{3}{2}}}{C}\frac{da_p}{dx}a_v(x),$$

$$\frac{\dot{\lambda}_i^\phi \mu_2}{r_i} = \frac{\kappa^{\frac{3}{2}}}{C}\frac{da_\lambda^\phi}{dx}a_v(x), \qquad \frac{\dot{\lambda}_i^v \mu_2}{r_i} = \frac{\kappa^{\frac{3}{2}}}{C}\frac{da_\lambda^v}{dx}a_v(x),$$

$$\frac{\dot{\lambda}_i^p \mu_2}{r_i} = \frac{\kappa^{\frac{3}{2}}}{C}\frac{da_\lambda^p}{dx}a_v(x) \tag{33}$$

When $m=3$, again, all variables are parallel to the Fiedler mode according to $v_{i,3}=b_v(x)r_i$, $p_{i,3}=b_p(x)r_i$, $\lambda_{i,3}^\phi = b_\lambda^\phi(x)r_i/\mu_2$, $\lambda_{i,3}^v = b_\lambda^v(x)r_i/\mu_2$, and $\lambda_{i,3}^p = b_\lambda^p(x)r_i/\mu_2$. Substituting into Eqs.(33), Eqs.(16-17) and

Eqs.(19-20), we find:

$$\frac{a_v}{C}\frac{da_v}{dx} = -\gamma b_v + b_p, \tag{34}$$

$$\frac{a_v}{C}\frac{da_p}{dx} = -\alpha b_p + b_\lambda^p, \tag{35}$$

$$\frac{a_v}{C}\frac{da_\lambda^v}{dx} = -b_\lambda^\phi + \frac{\gamma}{M}b_\lambda^v, \tag{36}$$

$$\frac{a_v}{C}\frac{da_\lambda^p}{dx} = \alpha b_\lambda^p - \frac{1}{M}b_\lambda^v. \tag{37}$$

Equation (34) requires elaboration. For SCSN, the coupling term is

$$\sum_j A_{ij}\sin(\phi_j-\phi_i) = \sum_j A_{ij}\sin(\phi_j^{SN}-\phi_i^{SN})+$$

$$C\kappa^{\frac{1}{2}}\big[1-\frac{5}{12}\kappa\big]x\sum_j A_{ij}\cos(\phi_j^{SN}-\phi_i^{SN})[r_j-r_i]-$$

$$\frac{C^2}{2!}\kappa\big[1-\frac{5}{12}\kappa\big]^2 x^2\sum_j A_{ij}\sin(\phi_j^{SN}-\phi_i^{SN})[r_j-r_i]^2-$$

$$\frac{C^3}{3!}\kappa^{\frac{3}{2}}\big[1-\frac{5}{12}\kappa\big]^3 x^3\sum_j A_{ij}\cos(\phi_j^{SN}-\phi_i^{SN})[r_j-r_i]^3 + ... \tag{38}$$

Note: all cosine terms vanish, since if i and j are in the same subgraph, then $r_i=r_j$, and if they are not, then $|\phi_j^{SN}-\phi_i^{SN}| = \frac{\pi}{2}$. This means, for instance, that $\bar{P}_i + K_{\mathrm{SN}}[1+\kappa]\sum_j A_{ij}\sin(\phi_j-\phi_i)$ only contains integer powers of κ.

To close the system, we again use the zero-energy condition at $\mathcal{O}(\kappa^{5/2})$. The resulting equation is:

$$\sum_i \bigg[\lambda_{i,3}^\phi v_{i,2} + \lambda_{i,2}^\phi v_{i,3} + \frac{1}{M}\lambda_{i,2}^v(-\gamma v_{i,3}+p_{i,3})$$

$$-\alpha p_{i,3}\lambda_{i,2} - \alpha p_{i,2}\lambda_{i,3} + \mu_2 \lambda_{i,2}^p \lambda_{i,3}^p\bigg]. \tag{39}$$

Substituting Eqs.(28-32) into Eqs.(34-37) and Eq.(39)

$$b_v = -\frac{2^{\frac{1}{2}}M}{\gamma^3}K_{\mathrm{SN}}^2 R_0^{\frac{3}{2}}R_2^{\frac{1}{2}}x[1-x^2] \tag{40}$$

$$b_p = -\frac{2^{\frac{3}{2}}M}{\gamma^2}K_{\mathrm{SN}}^2 R_0^{\frac{3}{2}}R_2^{\frac{1}{2}}x[1-x^2] \tag{41}$$

$$b_\lambda^\phi = 0, \tag{42}$$

$$b_\lambda^v = -\frac{2^{\frac{3}{2}}M^2\alpha^2}{\gamma^2}K_{\mathrm{SN}}^2 R_0^{\frac{3}{2}}R_2^{\frac{1}{2}}x[1-x^2], \tag{43}$$

$$b_\lambda^p = -\frac{2^{\frac{3}{2}}}{\gamma}\Big[1+\frac{M\alpha}{\gamma}\Big]K_{\mathrm{SN}}^2 R_0^{\frac{3}{2}}R_2^{\frac{1}{2}}x[1-x^2]. \tag{44}$$

In order to calculate the action at next order, $\mathcal{O}(\kappa^{5/2})$, we need to know $\lambda_{i,4}^\phi$. This can be achieved using Eqs.(40-44) and the zero-energy condition at $\mathcal{O}(\kappa^3)$. If

we assume $\lambda_{i,4}^{\phi} \sim r_i$, then the calculation only requires a fair bit of algebra. The result is:

$$\frac{\lambda_{i,4}^{\phi}}{r_i} = -\frac{4R_0^2 \gamma \alpha^3 K_{\mathrm{SN}}^2 \mu_3 [1-x^2]^2 \sum_i r_i^3}{3\mu_2^3}$$
$$- \frac{4R_0^2 R_2 K_{\mathrm{SN}}^3 x^2 [1-x^2]}{\gamma \mu_2}$$
$$- \frac{\gamma \alpha^2 K_{\mathrm{SN}} R_2^{\frac{1}{2}} x^2 [1-x^2]}{3R_0^{\frac{1}{2}} \mu_2}. \tag{45}$$

Note, that all constants in Eq.(45) can be given a closed-form expression for SCSN, and depend only on $|\mathcal{S}_1|$ and $|\mathcal{S}_2|$. In Fig.5 we show the accuracy of our expansion for the UK grid with a SCSN, Fig.3(b)(top). Solutions of Eqs.(11) are shown in blue at $\kappa = 0.001$. In panel (a) the $\mathcal{O}(\kappa)$ solution, Eqs.(8), is shown in red. In panel (b), we show the error of Eqs.(8) compared to the $\mathcal{O}(\kappa^2)$ solution, Eq.(45). The agreement is excellent at both orders of κ.
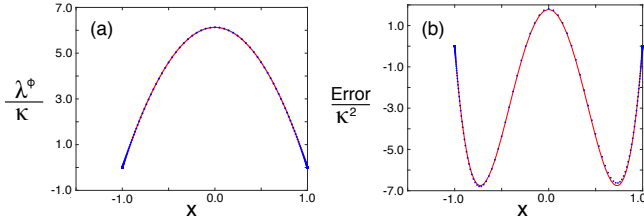

FIG. 5. Near bifurcation comparison for SCSN. Computed paths are shown in blue from Eqs.(11). (a) $\mathcal{O}(\kappa)$ solution, (red) Eqs.(8). (b) $\mathcal{O}(\kappa^2)$ solution (blue) Eq.(45).

Integrating our expressions for the phase-space variables to $\mathcal{O}(\kappa^2)$ in λ_i^{ϕ} and $\mathcal{O}(\kappa^{\frac{3}{2}})$ for all others, according to Eq.(6), gives the action for SCSN at $\mathcal{O}(\kappa^{\frac{5}{2}})$.

VI. Non-Gaussian effects

We would like to know how the higher-moments of the power-increment distribution contribute to the action in general. As in the main text, we restrict ourselves to *iid* power fluctuations. A clue comes from our solution for the OP at lowest order in κ. Recall from Sec.V, that $\lambda_{i,2}^{\phi}$ is determined by the zero-energy condition at $\mathcal{O}(\kappa^2)$ – where the noise variance μ_2 first appears in $H(\boldsymbol{\phi}, \mathbf{v}, \mathbf{p}, \boldsymbol{\lambda}^{\phi}, \boldsymbol{\lambda}^v, \boldsymbol{\lambda}^p)$. We can check if this pattern is repeated for μ_3, by looking at $H(\boldsymbol{\phi}, \mathbf{v}, \mathbf{p}, \boldsymbol{\lambda}^{\phi}, \boldsymbol{\lambda}^v, \boldsymbol{\lambda}^p) = 0$ at $\mathcal{O}(\kappa^3)$. Using our general expansion, we get an equa-

tion:

$$0 = \sum_i \left[\lambda_{i,4}^{\phi} v_{i,2} + \lambda_{i,3}^{\phi} v_{i,3} + \lambda_{i,2}^{\phi} v_{i,4} + \frac{1}{M}\lambda_{i,4}^v T_{i,2} + \right.$$
$$\frac{1}{M}\lambda_{i,3}^v T_{i,3} + \frac{1}{M}\lambda_{i,2}^v T_{i,4} - \alpha \lambda_{i,4}^p p_{i,2} - \alpha \lambda_{i,3}^p p_{i,3} -$$
$$\left. \alpha \lambda_{i,2}^p p_{i,4} + \mu_2 \lambda_{i,2}^p \lambda_{i,4}^p + \frac{\mu_2}{2}[\lambda_{i,3}^p]^2 + \frac{\mu_3}{3!}[\lambda_{i,2}^p]^3 \right]. \tag{46}$$

Note, we have introduced the notation $T_i \equiv -\gamma v_i + p_i + \bar{P}_i + K \sum_j A_{ij} \sin(\phi_j - \phi_i)$ and $T_i = \sum_m T_{i,m} \kappa^{\frac{m}{2}}$.

It is important to realize a few properties of the phase-space coordinates. First, only the conjugate momenta, (the λ's), depend explicitly on the noise statistics. Second, since $\mathcal{O}(\kappa^n)$ is the lowest order at which μ_n enters the Hamiltonian, $\lambda_{i,2n-j}^{\phi}$, $\lambda_{i,2n-j}^v$, and $\lambda_{i,2n-j}^p$ $\forall (1 \leq j < 2n-1)$ depend on $\mu_{n-1}, \mu_{n-2}, ... \mu_2$, but not on μ_n. Therefore, if $\lambda_{i,4}^v$ and $\lambda_{i,4}^p$ vanish from Eq.(46), then only two terms depend on μ_3, and we can solve explicitly for the contribution to $\lambda_{i,4}^{\phi}$ from μ_3.

Luckily, the terms proportional to $\lambda_{i,4}^v$ and $\lambda_{i,4}^p$ in Eq.(46) depend on the lowest order solution, which we have explicit expressions for. In fact, $T_{i,2} = 0$ and $-\alpha p_{i,2} + \mu_2 \lambda_{i,2}^p = 0$. Finally, we add an additional assumption that $\lambda_{i,4}^{\phi} \sim r_i$, as with the SCSN, Eq.(45). With this assumption, the lowest-order (in κ) contribution to λ_i^{ϕ} from μ_3, denoted $\Delta^{(3)}\lambda_i^{\phi}$ is found from Eq.(46):

$$\frac{\Delta^{(3)}\lambda_i^{\phi}}{r_i} = -\frac{\mu_3 \sum_j [\lambda_{j,2}^p]^3}{3! \sum_j r_j v_{j,2}}. \tag{47}$$

Exactly the same argument can be used to calculate $\Delta^{(4)}\lambda_i^{\phi}$, etc. The general expression is

$$\frac{\Delta^{(n)}\lambda_i^{\phi}}{r_i} = -\frac{\mu_n \sum_j [\lambda_{j,2}^p]^n}{n! \sum_j r_j v_{j,2}}. \tag{48}$$

The lowest-order contribution to the action from μ_n is found from Eq.(6) – namely, integrating $\Delta^{(n)}\lambda_i^{\phi}(x)$ over x. The result is Eq.(10) in the main text. Note: the integral contributions from λ_i^v and λ_i^p can be ignored, since v_i and p_i are at lowest order $\mathcal{O}(\kappa)$, while $\phi_i^s - \phi_i^*$ is $\mathcal{O}(\kappa^{1/2})$.

Equation (10) can be used to compare the actions of two increment distributions that differ in the nth moment. For instance, the difference in the action between a symmetric increment distribution ($\mu_3 = 0$) and a non-symmetric distribution ($\mu_3 \neq 0$), each with the same variance μ_2, is given by Eq.(10) with $n = 3$.

Furthermore, as noted in the main text, if the power fluctuations are assumed to be Gaussian white noise with a variance μ_2, then Eq. (10) gives the exponential correction to the rate of desynchronization for non-symmetric ($n = 3$), and symmetric ($n = 4$) increment distributions. For Gaussian white noise, the equations of motion are

identical except for Eq.(17):

$$\dot{p}_i \stackrel{\text{Guass}}{=} -\alpha p_i + \mu_{i,2}\lambda_i^p, \qquad (49)$$

and the Hamiltonian Eq.(5):

$$H(\boldsymbol{\phi}, \mathbf{v}, \mathbf{p}, \boldsymbol{\lambda}^\phi, \boldsymbol{\lambda}^v, \boldsymbol{\lambda}^p) \stackrel{\text{Guass}}{=} \sum_i \Bigg[\lambda_i^\phi v_i - \alpha p_i \lambda_i^p + \frac{\mu_{i,2}}{2}[\lambda_i^p]^2$$

$$+ \frac{\lambda_i^v}{M}\Big(-\gamma v_i + \bar{P}_i + p_i + \sum_j K_{ij}\sin(\phi_j - \phi_i)\Big)\Bigg]. \qquad (50)$$

VII. Synchronized subgraph approximation

As mentioned in the main text, in many cases the SN bifurcation occurs with exact symmetry in the Fiedler mode; namely, the network is partitioned into $\mathcal{N}$ subgraphs, $\mathcal{S}_1, \mathcal{S}_2, ..., \mathcal{S}_\mathcal{N}$, where two nodes i and j in the same subgraph $\mathcal{S}_n$ have $r_i = r_j = r^{(n)}$ at bifurcation. As already noted, SCSN cases have $\mathcal{N} = 2$, including trees. Larger values of $\mathcal{N}$ occur for block-networks (or clique trees), such as Fig.3(b)–the lower panel.

Since, the Fiedler mode is the weakest stable mode of the network and the optimal desynchronization path is parallel to r_i over several orders in κ, as demonstrated in previous sections, we simply assume (as an approximation) that all nodes within the same subgraph, e.g., n, are synchronized: $\phi_i - \phi_i^{SN} = \Phi_n$, $v_i = \mathcal{V}_n$, $p_i = \mathcal{P}_n$, $\lambda_i^\phi = l_n^\phi$, $\lambda_i^v = l_n^v$, and $\lambda_i^p = l_n^p \; \forall i \in \mathcal{S}_n$. We can find an approximate set of Hamilton's equations for such OPs by simply averaging over all nodes within a subgraph:

$$\dot{\Phi}_n = \sum_{i\in\mathcal{S}_n}\frac{\dot{\phi}_i}{|\mathcal{S}_n|}, \quad \dot{\mathcal{V}}_n = \sum_{i\in\mathcal{S}_n}\frac{\dot{v}_i}{|\mathcal{S}_n|},$$

$$\dot{\mathcal{P}}_n = \sum_{i\in\mathcal{S}_n}\frac{\dot{p}_i}{|\mathcal{S}_n|}, \quad \dot{l}_n^\phi = \sum_{i\in\mathcal{S}_n}\frac{\dot{\lambda}_i^\phi}{|\mathcal{S}_n|}$$

$$\dot{l}_n^v = \sum_{i\in\mathcal{S}_n}\frac{\dot{\lambda}_i^v}{|\mathcal{S}_n|} \quad \dot{l}_n^p = \sum_{i\in\mathcal{S}_n}\frac{\dot{\lambda}_i^p}{|\mathcal{S}_n|}. \qquad (51)$$

So far Eqs.(51) leaves us with coupling terms

$$\mathcal{X}_n = \sum_{i\in\mathcal{S}_n, j\notin\mathcal{S}_n} A_{ij}\sin(\phi_j - \phi_i) \quad \text{and} \qquad (52)$$

$$\mathcal{Y}_n = \sum_{i\in\mathcal{S}_n, j\notin\mathcal{S}_n} A_{ij}\cos(\phi_j - \phi_i)[\lambda_j^v - \lambda_i^v] \qquad (53)$$

Let us specify an index function which maps the node number i to its subgraph number n, i.e., $F(i) = n$. Using this notation, the coupling terms become:

$$\mathcal{X}_n = \sum_{i\in\mathcal{S}_n, j\notin\mathcal{S}_n} A_{ij}\Big[\sin(\phi_j^{SN} - \phi_i^{SN})\cos(\Phi_{F(j)} - \Phi_{F(i)})$$

$$+ \cos(\phi_j^{SN} - \phi_i^{SN})\sin(\Phi_{F(j)} - \Phi_{F(i)})\Big] \qquad (54)$$

$$\mathcal{Y}_n = \sum_{i\in\mathcal{S}_n, j\notin\mathcal{S}_n} A_{ij}\Big[\cos(\phi_j^{SN} - \phi_i^{SN})\sin(\Phi_{F(j)} - \Phi_{F(i)})[l_{F(j)}^v - l_{F(i)}^v]$$

$$- \sin(\phi_j^{SN} - \phi_i^{SN})\cos(\Phi_{F(j)} - \Phi_{F(i)})[l_{F(j)}^v - l_{F(i)}^v]\Big]. \qquad (55)$$

Now, since all phase-space variables are assumed to be synchronized within subgraphs, we can define the following effective coupling matrices between subgraphs n and n'

$$S_{nn'} = \sum_{i\in\mathcal{S}_n, j\in\mathcal{S}_{n'}} A_{ij}\sin(\phi_j^{SN} - \phi_i^{SN}), \qquad (56)$$

$$C_{nn'} = \sum_{i\in\mathcal{S}_n, j\in\mathcal{S}_{n'}} A_{ij}\cos(\phi_j^{SN} - \phi_i^{SN}). \qquad (57)$$

Therefore, the synchronized subgraph equations become

$$\dot{\Phi}_n = \mathcal{V}_n, \qquad (58)$$

$$M\dot{\mathcal{V}}_n = -\gamma\mathcal{V}_n + \mathcal{P}_n + \sum_{i\in\mathcal{S}_n}\frac{\bar{P}_i}{|\mathcal{S}|} +$$

$$\frac{K_{\text{SN}}[1+\kappa]}{|\mathcal{S}|}\sum_{n'\neq n} S_{nn'}\cos(\Phi_{n'} - \Phi_n) + C_{nn'}\sin(\Phi_{n'} - \Phi_n), \qquad (59)$$

$$\dot{\mathcal{P}}_n = -\alpha\mathcal{P}_n + \sum_m \nu_m g_m \exp\{g_m l_n^p\} \qquad (60)$$

$$\dot{l}_n^\phi = -\frac{K_{\text{SN}}[1+\kappa]}{M|\mathcal{S}|}\sum_{n'\neq n}\Bigg[C_{nn'}\cos(\Phi_{n'} - \Phi_n)[l_{n'}^v - l_n^v]$$

$$- S_{nn'}\sin(\Phi_{n'} - \Phi_n)[l_{n'}^v - l_n^v]\Bigg], \qquad (61)$$

$$\dot{l}_n^v = -l_n^\phi + \frac{\gamma}{M}l_n^v, \qquad (62)$$

$$\dot{l}_n^p = \alpha l_n^p - l_n^v/M. \qquad (63)$$

In general, the matrices Eqs.(56-57) have to be computed numerically at the saddle-node bifurcation in order to solve Eqs.(58-63).

However, for SCSN the results simplify significantly. In this case $n = 1, 2$, and $C_{2,1} = C_{1,2} = 0$ and $S_{2,1} = -S_{1,2} = 1$. In addition, we notice that the effective two-oscillator system for SCSN can be reduced to one by introducing the relative coordinates: $\Psi = \Phi_1 - \Phi_2$, $V = \dot{\Psi}$, $P = \mathcal{P}_1 - \mathcal{P}_2$, $\Lambda_\Psi = |\mathcal{S}_1|l_1^\phi = -|\mathcal{S}_2|l_2^\phi$, $\Lambda_V = |\mathcal{S}_1|l_1^v = -|\mathcal{S}_2|l_2^v$, and $\Lambda_P = |\mathcal{S}_1|l_1^p = -|\mathcal{S}_2|l_2^p$. The result is Eqs.(11) in the main text.

Equations (58-63) can be used as a coarse-grained approximation for networks without exact symmetry in the Fiedler mode. One simply groups together nodes in a subgraph if they have similar values, where similar means within some tolerance. An example is shown in Fig.6, for the UK power-grid example from Fig.3 without symmetry (magenta). Plotted is the Fiedler mode at bifurcation versus the node number. Blue, magenta, green, and cyan
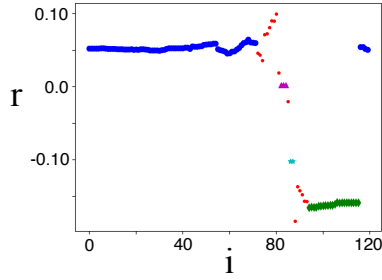
FIG. 6. Fiedler mode at bifurcation for the UK grid-example from Fig.3 without symmetry (magenta). Blue, magenta, green, and cyan nodes were placed in the same subgraphs, since their values are within 5%. Each of the red nodes was treated as a subgraph.

nodes were placed in the same subgraphs, since their values are within 5%. Each of the red nodes was treated as a subgraph (of size one). The total number of subgraphs is twenty. The coupling matrices Eqs.(56-57) were computed at bifurcation given this binning, and the OPs were solved from Eqs.(58-63) with twenty subgraphs.

[1] A. Arenas, A. Diaz-Guilera, J. Kurths, Y. Moreno, and C. Zhou, Phys. Rep. **469**, 93 (2008).
[2] F. Dörfler, M. Chertkov, and F. Bullo, Proc. Natl. Acad. Sci. U.S.A., **110**, 2005 (2013).
[3] R. F. Voss and R. A. Webb, Phys. Rev. B **25**, 3446 (1982).
[4] A. Buzdin, Phys. Rev. Lett. **101**, 107005 (2008).
[5] A. M. Hagerstrom, T. E. Murphy, R. Roy, P. Hovel, I. Omelchenko, E. Scholl, Nature Physics **8**, 658 (2012).
[6] J. T. Buchanan, Biological Cybernetics **66**, 367 (1992).
[7] J. Buck, Quarterly Review of Biology **63**, 265 (1988).
[8] S. M. Crook, G. B. Ermentrout, M. C. Vanier, Journal of Computational Neuroscience **4**, 161 (1997).
[9] R. E. Mirollo and S. H. Strogatz, Siam Journal on Applied Mathematics **50**, 1645 (1990).
[10] A. J. Ijspeert, Neural Networks **21**, 642 (2008).
[11] E. A. Martens, S. Thutupalli, A. Fourriere, O. Hallatschek, Proc. Natl. Acad. Sci. U.S.A., **110**, 10563 (2013).
[12] M. A. Zhang, G. S. Wiederhecker, S. Manipatruni, A. Barnard, P. McEuen, and M. Lipson, Phys. Rev. Lett. **109**, 233906 (2012).
[13] H. Ronellenfitsch, J. Dunkel, and M. Wilczek, Phys. Rev. Lett. **121**, 208301 (2018).
[14] B. Schäfer, M. Matthiae, X. Zhang, M. Rohden, M. Timme, and D. Witthaut, Phys. Rev. E **95**, 060203(R) (2017).
[15] J. Creaser, K. Tsaneva-Atanasova, and P. Ashwin, SIAM J. Appl. Dyn. Syst. **17**, 500 (2018).
[16] J. Hindes and I. B. Schwartz, Chaos **28**, 071106 (2018).
[17] L. DeVille, Nonlinearity **25**, 1473 (2012).
[18] M. Tyloo, R. Delabays, and P. Jacquod, arXiv:1812.09497 [nlin.AO] (2018).
[19] X. Zhang, S. Hallerberg, M. Matthiae, D. Witthaut, and M. Timme, arXiv:1809.03081 [nlin.AO] (2018).
[20] J. Lipinski-Kruszka, J. Stewart-Ornstein, M. W. Chevalier, and H. El-Samad, ACS Synth. Biol. **4**, 258 (2015).
[21] H. Haehne, K. Schmietendorf, S. Tamrakar, J. Peinke, and S. Kettemann, arXiv:1809.09098v2 [physics.soc-ph] (2019).
[22] Y. Kawamura and H. Nakao, Phys. Rev. E **94**, 032201 (2016).
[23] Q. Guo and F. Wan, PLOS ONE **12**, 12 (2017).

[24] P. Milan, M. Wächter, and J. Peinke, Phys. Rev. Lett. **110**, 138701 (2013).
[25] M. Anvari, G. Lohmann, M. Wächter, P. Milan, E. Lorenz, D. Heinemann, M. R. R. Tabar, and J. Peinke, New J. Phys. **18**, 063027 (2016).
[26] B. Schäfer, C. Beck, K. Aihara, D. Witthaut, and M. Timme, Nature Energy bf 3, 119 (2018).
[27] J. Ankerhold, *Counting Electrical charges: a problem of thermal escape and quantum tunneling in presence of non-Gaussian noise*, Path Integrals: New Trends and Perspectives, Proceedings, 435-442 (2008).
[28] H. Grabert, Phys. Rev. B **77**, 205315 (2008).
[29] I. A Khovanov and N. A. Khovanova, Phys. Rev. B **89**, 085419 (2014).
[30] E. V. Sukhorukov, A. N. Jordan, Physica E: Low-dimensional Systems and Nanostructures **42**, 550 (2010).
[31] D. Valenti, C. Guarcello, and B. Spagnolo, Phys. Rev. B **89**, 214510 (2014).
[32] J. Zou, S. Buvaev, M. Dykman, H. B. Chan, Phys. Rev. B **86**, 155420 (2012).
[33] K. Schmientendorf, J. Peinke, and O. Kamps, arXiv:1611.08235 [nlin.AO] (2016).
[34] S. Pahwa, C. Scoglio, A. Scala, Sci. Rep.**4**, 2045 (2014).
[35] S. Auer, F. Hellmann, M. Krause, and J. Kurths, Chaos **27**, 127003 (2017).
[36] T. Nesti, A. Zocca, and B. Zwart, Phys. Rev. Lett. **120**, 258301 (2018).
[37] Equation 1 is dimensionless– normalized by rated power. The inertia and damping constants are fixed[14]: $M = 0.02546s^2$ and $\gamma = 0.10053s$. The average powers, $\bar{P}_i$, are independent, identically, and uniformly distributed over the interval $[-0.5, 0.5]$. The power-damping rate, α, was taken to range from $0.25s^{-1}$ to $1s^{-1}$.
[38] T. Nishikawa T and A. E. Motter, New Journal of Physics **17**, 015012 (2015).
[39] J. Machowski, J. Bialek, and J. R. Bumby, *Power system dynamics: stability and control* (John Wiley & Sons, 2008), 2nd ed.
[40] T. Coletta, B. Bamieh, and Ph. Jacquod, arXiv:1807.09048 [math.OC].
[41] R. P. Feynman and A. R. Hibbs. *Quantum Mechanics and Path Integrals* (Dover Publications, New York, 2010), emended edition.

[42] The time constant for the wind-turbine fluctuations was chosen to be a factor of ten smaller than the original data, so that a wider range of parameters could be explored.

[43] D. Manik, D. Witthaut, B. Schäfer, M. Matthiae, A. Sorge, M. Rohden, E. Katifori, and M. Timme, Eur. Phys. J. Special Topics **223**, 2527 (2014).

[44] H. Kramers, Physica **7**, 284 (1940).

[45] M. I. Dykman, Phys. Rev. A **42**, 2020 (1990).

[46] L. Billings, I. B. Schwartz, M. McCrary, A.N. Korotkov, M. I. Dykman, Phys. Rev. Lett. **104**, 140601 (2010).

[47] M. I. Dykman, Phys. Rev. E **81**, 051124 (2010).

[48] See supplementary material for further details.

[49] The energy along the optimal path is zero since there is no explicit time dependence in Eqs.(1-3).

[50] B. S. Lindley and I. B. Schwartz, Physica D **255**, 25 (2013).

[51] M. I. Dykman, E. Mori, J. Ross, and P. M. Hunt, J. Chem. Phys. **100**, 5735 (1994).

[52] M. Fiedler, Czechoslovak Mathematical Journal **23**, 298 (1973).

[53] A. H. Dekker and R. Taylor, SIAM J. Appl. Dyn. Syst. **12**, 596 (2013).

[54] M. Assaf and B. Meerson, Phys. Rev. E **81**, 021116, (2010).

[55] J. Hindes and I. B. Schwartz, Phys. Rev. Lett. **117**, 028302 (2016).

[56] L. Böttcher, M. Luković, J. Nagler, S. Havlin, H. J. Herrmann, Sci. Rep. **7**, 41729 (2017).

[57] S. A. M. Loos, J. C. Claussen, E. Schöll, and A. Zakharova Phys. Rev. E **93**, 012209 (2016).